CHALMERS

Research report - Department of Mechanics and Maritime Sciences 2019:02

Wind tunnel & CFD investigations of ICE3 train

Project in Applied Mechanics 2019

Department of Mechanics and Maritime Sciences
CHALMERS UNIVERSITY OF TECHNOLOGY
Göteborg, Sweden 2019

Wind tunnel & CFD investigations of ICE3 train
Project in Applied Mechanics 2019

Research report - Department of Mechanics and Maritime Sciences 2019:02

Department of Mechanics and Maritime Sciences
Chalmers University of Technology
SE-412 96 Göteborg
Sweden
Telephone +46 (0)31 772 1000

Preface

The work in the present report was carried out as a part of the course TME131 Project in Applied Mechanics, which is a mandatory course within the Applied Mechanics Masters programme at Chalmers. The course was carried out during spring semester 2019.

Abstract

Cruise speeds of trains have steadily increased over the years. These high cruise speeds, in the order of 300 km/h, lead to high values of drag, a significant wake region behind the train and high noise levels (90 - 100dBA). While the high drag directly affects the performance of the train, the wake region and the noise levels can have a hazardous effect on the neighbouring areas through which the rail-line passes and on the ground workers. Therefore addressing these issues is of utmost importance. This is where aerodynamics and flow visualization plays a significant role. CFD simulation provides a powerful tool to achieve these things. However, the validity of CFD models first needs to be established against experimental values. In this project such a CFD model is created. A simplified scale model of an ICE3 train is also manufactured and is used to verify the CFD model. The pressure is obtained at different points using pressure taps on the experimental model during wind tunnel testing. Then, a comparison of the normalized pressure coefficients is made between the experimental and the numerical model to verify the validity of the latter. Once the numerical model is established, it is used to analyze the influence of the ground clearance on the train. It was found that the increase in the ground clearance resulted in higher drag and lift forces experienced by the train.

Contents

1 Introduction

In this project a physical model of an ICE3 train is built and tested in a wind tunnel. Computational calculations are also carried out and compared to the wind tunnel data. The importance of numerical and real world correlation is investigated.

1.1 Background

The ICE3 or the Inter-City Express 3, is a high speed train manufactured by Siemens and operated and owned by Nederlandse Spoorwegen (NS, Dutch Railways) and Deutsche Bahn (DB, German Railways) from the year 2000 to present. As cruise speeds for trains increase, so does the importance of the aerodynamic package since the drag varies with the square of the velocity. High cruise speeds also result in a wake region behind the train which can cause safety related issues for nearby ground workers. Furthermore, high cruise speeds lead to high noise levels in the order of 90-100 dBA, if the body of the train is not specifically designed to reduce the noise. These high noise levels have a hazardous effect on the neighbourhoods through which the train passes. According to the National Institute on Deafness and Other Communication Disorders as cited in [1], noise levels above 85 dBA can cause hearing loss on long exposure. Therefore, understanding the flow becomes of great importance to predict the aforementioned effects. To make these predictions, good accuracy in CFD is required. This is acquired from comparison with experimental measurements such as wind tunnel experiments. Similar models of other trains have for instance been used to do research on the wake region [2], the effect of the yaw angle [3] and the influence of bogies [4].

1.2 Project goals

The project aims to create a simplified physical model of an ICE3 train. The model is used for experimental measurements in a wind tunnel experiment. The data from the experiment is used to verify CFD simulations. The CFD simulations are carried out in STAR-CCM+. In particular, the drag coefficient on the entire model, and the pressure coefficients at certain points of the model will be considered. Finally, the verified model is used to determine the influence of the ground clearance on the drag and lift forces of the train.

2 Theory

2.1 Drag and pressure coefficient

The experimental test and the numerical model will result in drag force values and pressures values at certain points on the surface of the model. In order to more accurately compare these results, the drag coefficient and the pressure coefficient will be compared instead. These coefficients are dimensionless parameters that take into account any other dissimilarities between the models that could lead to a difference in drag force or pressure, for instance small deviations in velocity.

The drag force, F_d, is normalized by the density of the fluid, ρ, the incoming flow velocity, u, and the frontal area of the train, A. The frontal area of the train is the area that is normal to the flow direction. This results in the following definition for the drag coefficient, c_d,

$$c_d = \frac{2F_d}{\rho u^2 A}. \tag{1}$$

The pressure, p, is normalized by the free-stream velocity and density, u_∞ and ρ_∞. Furthermore, the free-stream pressure, p_∞, which is the same as the static pressure far upstream of the train, is used as a reference pressure. This results in a pressure coefficient, c_p, defined as

$$c_p = \frac{p - p_\infty}{\frac{1}{2}\rho_\infty u_\infty^2}. \tag{2}$$

2.2 Reynolds number

In this project a scaled model of the ICE3 train is created. In order to ensure that this scaling does not affect the fluid flow, the Reynolds number is calculated. This is a reference dimensionless quantity that is used to reproduce the same flow conditions. Keeping the flow conditions the same is important when working with differently scaled models, such as in this project. The Reynolds number needs to be such that, the predicted flow is the same both in the scaled as in the unscaled case.

The Reynolds number is defined as

$$\mathrm{Re} = \frac{u \times L}{\nu}. \tag{3}$$

In the above equation u is the inlet velocity of the flow, L is the characteristic length of the object and ν is the kinematic viscosity of the fluid. The height of the train model is taken as the characteristic length, as this is the largest length scale normal to the direction of the flow.

First the Reynolds number for the real train is calculated. A full scale ICE3 train has a height of 3.7 m. The maximum velocity of the train is 320 km/h, or 88.9 m/s [5]. This means that in the reference frame where the train stands still the fluid will move with 320 km/h towards it. The kinematic viscosity of air under atmospheric conditions (25°C and 1 bar) is 15.5×10^{-6} m^2/s. This results in a Reynolds number of

$$Re = \frac{u \times L}{\nu} = \frac{88.9 \times 3.7}{15.5 \times 10^{-6}} = 21 \times 10^6. \tag{4}$$

Here it is important to note that the Reynolds number only affects the flow up to $Re = 250\,000$ [6]. Therefore that is the minimum Reynolds number we can use for the observation and calculation of the flow around

the scale model, without decreasing the accuracy of the results. The height of the scale model, and thus its characteristic length, is given in the project description as 0.1815 m. Since the dynamic viscosity does not change it is used to calculate the minimum velocity of the flow in the wind tunnel. This velocity is

$$u = \frac{Re \times \nu}{L} = \frac{250\,000 \times 15.5 \times 10^{-6}}{0.1815} = 21.3\text{m/s}. \tag{5}$$

2.3 RANS

Viscous fluid quantities are governed by the Navier-Stokes equations. This means that by solving the Navier-Stokes equations one can model the flow throughout a domain, given that the mesh in the domain is fine enough. However, for more complex models, such as the one used in this project, it is not possible to use a sufficiently fine mesh, due to computational limits. Therefore the RANS model is introduced, which models the turbulent flow and thus reduces the necessary computational time. In the RANS model the flow is decomposed into the mean flow and its fluctuations [7]. This decomposition is defined as

$$\phi = \overline{\phi} + \phi'. \tag{6}$$

Here the overline represents the time averaged value, whereas the apostrophe denotes the fluctuations. Note that ϕ is simply a placeholder and can be replaced by any quantity, e.g. pressure or velocity.

Using this decomposition the mean Navier-Stokes equations can be determined. These are the mean mass and momentum transport equations and are given, respectively, as [7]

$$\frac{\partial \rho}{\partial t} + \nabla \cdot (\rho \overline{\mathbf{v}}) = 0, \tag{7}$$

$$\frac{\partial}{\partial t}(\rho \overline{\mathbf{v}}) + \nabla \cdot (\rho \overline{\mathbf{v}} \otimes \overline{\mathbf{v}}) = -\nabla \overline{p}\mathbf{I} + \nabla \cdot (\mathbf{T} + \mathbf{T_{RANS}}) + \mathbf{F_b}. \tag{8}$$

Here I is the identity tensor, T is the viscous stress tensor and $\mathbf{F_b}$ is the resultant of any present body forces, e.g. gravity. $\mathbf{v}$ is the vector of velocities, u, v and w. The problem with these equations is the Reynolds stress tensor, $\mathbf{T_{RANS}}$. This tensor is, in tensor notation, defined as [7]

$$\mathbf{T_{RANS}} = \rho \overline{\mathbf{v_i'} \mathbf{v_j'}} + \frac{\mathbf{2}}{\mathbf{3}} \rho \mathbf{k} \delta_{\mathbf{ij}} \tag{9}$$

There is no way to calculate these values and therefore they need to be modeled. There are two ways of doing this. The first is to solve transport or algebraic modeled equation for each Reynolds stress [8]. These models are the RSM and ASM, which stands for Reynolds stress transport model and Algebraic Reynolds stress model, respectively.

The second method is based on the Boussinesq assumption and uses the eddy viscosity [8]. These models are called the eddy-viscosity models and they are widely used in turbulence modeling. Two of the most prominent in this group are the $k - \epsilon$ and $k - \omega$ turbulence models. In this project two models in this group are used.

2.3.1 Realizable $k-\epsilon$ two-layer

The $k-\epsilon$ model is a so called two-equation model. This means that the model is defined by two equations, in this case the modeled k-equation and the modeled ϵ-equation. Here k is the turbulent kinetic energy and ϵ is the dissipation of turbulent energy. Note that the description of the model and the definition of the equations in this section is based on the STAR-CCM+ documentation, unless specified otherwise [7]. In this project, a different version than the standard $k-\epsilon$ model is used, namely the realizable $k-\epsilon$ two-layer model. The realizable part means that the model contains a damping function on the constant c_μ. This lets the model satisfy constraints on the normal stresses consistent with turbulence. This eventuates in results that generally are at least as accurate as the standard $k-\epsilon$ model. The two-layer approach gives the model added flexibility for the y^+ treatment at the wall.

The modeled k-equation is defined as

$$\frac{\partial k}{\partial t} + \nabla \cdot (k\overline{\mathbf{v}}) = \nabla \cdot \left[\left(\nu + \frac{\nu_t}{\sigma_k} \right) \nabla k \right] + P_K - \epsilon. \tag{10}$$

Here P_K is the production term in the k-equation. It is defined as

$$P_K = f_c \left(\nu_t S^2 - \frac{2}{3} k \nabla \cdot \overline{\mathbf{v}} - \frac{2}{3} \nu_t \left(\nabla \cdot \overline{\mathbf{v}} \right)^2 \right) + \beta \frac{\nu_t}{Pr_t} \left(\nabla \overline{T} \cdot \mathbf{g} \right) + \frac{C_M k \epsilon}{c^2 \rho} + \nabla \cdot \overline{\mathbf{v}} : \left(\mathbf{T_{RANS,NL}} \right). \tag{11}$$

Here f_c is the curvature correction factor and S is the strain rate tensor. $\mathbf{T_{RANS,NL}}$ is the non-linear part of the Reynolds stress tensor and is given by the constitutive relation.

Similarly, the modeled ϵ-equation is defined as

$$\frac{\partial \epsilon}{\partial t} + \nabla \cdot (\epsilon \overline{\mathbf{v}}) = \nabla \cdot \left[\left(\nu + \frac{\nu_t}{\sigma_\epsilon} \right) \nabla \epsilon \right] + \frac{\epsilon}{k\rho} c_{\epsilon 1} P_\epsilon + c_{\epsilon 2} f_1 \frac{\epsilon^2}{k}. \tag{12}$$

P_ϵ is the product term and is defined as

$$P_\epsilon = f_c S k + C_{\epsilon 3} \beta \frac{\nu_t}{Pr_t} \left(\nabla \overline{T} \cdot \mathbf{g} \right). \tag{13}$$

Here Pr_t is the turbulent Prandtl number. f_1 is a damping function and is defined as

$$f_1 = \frac{k}{k + \sqrt{\nu \epsilon}}. \tag{14}$$

Finally, β is the thermal expansion coefficient and is defined as $\beta = T^{-1}$ [8]. $c_{\epsilon 3} = \tanh \frac{|\mathbf{v_b}|}{|\mathbf{u_b}|}$, where $\mathbf{v_b}$ and $\mathbf{u_b}$ are the velocity components parallel and perpendicular to the gravitational vector.

Finally, the turbulent viscosity in these equations is defined as

$$\nu_t = c_\mu f_\mu \frac{k^2}{\epsilon}, \tag{15}$$

where f_μ is a damping function.

For the coefficients standard values are used. These values correspond to

$$(c_\mu, c_{\epsilon 1}, c_{\epsilon 2}, \sigma_k, \sigma_\epsilon) = (0.09, 1.44, 1.9, 1, 1.2). \tag{16}$$

The $k-\epsilon$ model is one of the simpler models as it uses an isotropic eddy turbulent viscosity. However, it still works reasonably well for most engineering flows. One of the main advantages of the model is that it is very stable. The main disadvantage is that it is isotropic and thus incapable of predicting the normal stresses well. As a results, the model does not account properly for curvature effects and irrational strains, and will not be accurate when the boundary layer approaches separation [8].

2.3.2 $k-\omega$ SST

The $k-\omega$ model is a two equation model, similar to $k-\epsilon$. Instead of solving the diffusion equation for ϵ, as was the case in the $k-\epsilon$ model, the $k-\omega$ model solves the diffusion equation for the specific dissipation rate, ω. The SST in the $k-\omega$ SST model then stands for "Shear Stress Transport". In practice this means that the $k-\epsilon$ model is used near the wall and the $k-\omega$ model away from the wall. Once again the description of the model and the definition are based on the STAR-CCM+ documentation unless specified otherwise [7].

The equations for k and ω are given as

$$\frac{\partial k}{\partial t} + \nabla \cdot (k\overline{\mathbf{v}}) = \nabla \cdot \left[(\nu + \sigma_k \nu_t) \nabla k \right] + P^k - \beta^* k\omega \tag{17}$$

and

$$\frac{\partial \omega}{\partial t} + \nabla \cdot (\omega\overline{\mathbf{v}}) = \nabla \cdot \left[\left(\nu + \frac{\nu_t}{\sigma_\omega} \right) \nabla \omega \right] + P^\omega - \beta\omega^2. \tag{18}$$

Here P^k and P^ω are the source terms. These are defined as

$$P^k = f_c \nu_t S^2 - \frac{2}{3} k \nabla \cdot \overline{\mathbf{v}} - \frac{2}{3} \nu_t \left(\nabla \cdot \overline{\mathbf{v}} \right)^2 + \beta \frac{\nu_t}{Pr_t} \left(\nabla \overline{T} \cdot \mathbf{g} \right) + \nabla \cdot \overline{\mathbf{v}} : \left(\mathbf{T}_{\mathbf{RANS,NL}} \right), \tag{19}$$

$$P^\omega = \gamma \left[S^2 - \frac{2}{3} \omega \nabla \cdot \overline{\mathbf{v}} - \frac{2}{3} \left(\nabla \cdot \overline{\mathbf{v}} \right)^2 \right] + 2 \left(1 - f_2 \right) \sigma_{\omega 2} \frac{1}{\omega} \nabla k \cdot \nabla \omega. \tag{20}$$

Here f_2 is defined as

$$f_2 = \tanh \left(\left[\min \left(\max \left\{ \frac{\sqrt{k}}{\beta^* \omega d}, \frac{500\nu}{d^2 \omega} \right\}, \frac{2k}{CD_{k\omega} d^2} \right) \right]^4 \right). \tag{21}$$

Here $CD_{k\omega}$ is the cross-diffusion coefficient and is given as

$$CD_{k\omega} = \max \left\{ \frac{1}{\omega} \nabla k \cdot \nabla \omega, 10^{-20} \right\}. \tag{22}$$

Here d is the wall distance. The turbulent viscosity is now defined as

$$\nu_t = \frac{a_1 k}{\max \left(a_1 \omega, S f_3 \right)} \tag{23}$$

with

$$f_3 = \tanh\left[\left(\max\left\{\frac{2\sqrt{k}}{\beta^*\omega d}, \frac{500\nu}{d^2\omega}\right\}\right)^2\right] \tag{24}$$

Furthermore, γ, σ_k, σ_ω and β are given as follows

$$\phi = f_2\phi_1 + (1 - f_2)\,\phi_2 \tag{25}$$

where ϕ is a placeholder for γ, σ_k or σ_ω. γ_1 and γ_2 are then defined as

$$\gamma_i = \frac{\beta_i}{\beta^*} - \sigma_{\omega i}\frac{\kappa^2}{\sqrt{(\beta^*)}}. \tag{26}$$

Here $i = 1$ or $i = 2$. Finally, the additional constants are given as

$$(\sigma_{k1}, \sigma_{k2}, \sigma_{\omega_1}, \sigma_{\omega_2}, \beta_1, \beta_2, a_1, \kappa) = (0.85, 1, 0.5, 0.856, 0.075, 0.0828, 0.31, 0.41) \tag{27}$$

The $k - \omega$ SST model is a very accurate model for all flows involving adverse pressure gradients and is therefore an obvious choice as the model of use in this project [9]. However, a downside is that the model is less stable than the $k - \epsilon$ model, as the $k - \omega$ model is used for large portions of the flow.

2.4 Boundary layers

y^+ is the distance to the wall, non-dimensionalized using the kinematic viscosity and the friction velocity. It is used for calculating the distance in the wall normal direction from the first cell at the boundary layer according to [10]

$$u_* = \sqrt{\frac{\tau_{wall}}{\rho}} \tag{28}$$

$$n = \frac{\nu y^+}{u_*} \tag{29}$$

where u_* is the friction velocity, τ_{wall} is the wall shear stress and n is the distance between the center of the first cell and the wall. As an approximation $u_* = 0.05 * u_\infty$ where u_∞ is the free stream velocity.

Additionally the cell length in the streamwise direction, Δ_s, and in the spanwise direction, Δ_l, can be calculated according to [11]

$$\Delta_s = \frac{\nu\Delta_s^+}{u_*} \tag{30}$$

$$\Delta_l = \frac{\nu\Delta_l^+}{u_*} \tag{31}$$

where Δ_s^+ and Δ_l^+ are non-dimensional. As a rule regarding the mesh resolution when using RANS is $\Delta_s^+ < 1000$ and $\Delta_l^+ < 300$. The reason for the limit on Δ_s^+ and Δ_l^+ being different is based on the size of the eddies. The dimension of the eddies in the streamwise direction is higher than in the spanwise direction. Thus, a finer mesh, or higher resolution of the mesh, in the spanwise direction is require. This requirement is reflected in the limits for Δ_l^+, which is far lower than Δ_s^+, to ensure a finer mesh in the spanwise direction.

2.5 Pressure: types and measurements

In this report a number of different pressures are used. In this chapter these pressures and their differences are briefly explained.

There are three types of pressures that are relevant to the project; the dynamic, static and stagnation pressure. The dynamic pressure is the pressure caused by the movement of the fluid and is calculated as

$$p_{dyn} = \frac{1}{2}\rho u^2 \tag{32}$$

where ρ is the density and u is the velocity. The dynamic pressure is not directly measured but calculated from the other two pressures using

$$p_{dynamic} = p_{stagnation} - p_{static} \tag{33}$$

The static pressure is the pressure exerted on the body when at rest [12]. The stagnation pressure is the pressure at a point at which the flow comes to a complete stop, for example at far front point of a ball flying in a straight line. In an incompressible flow with no gravitational effects it is constant in the domain. The static and stagnation pressure can be measured as shown in Figure 1.

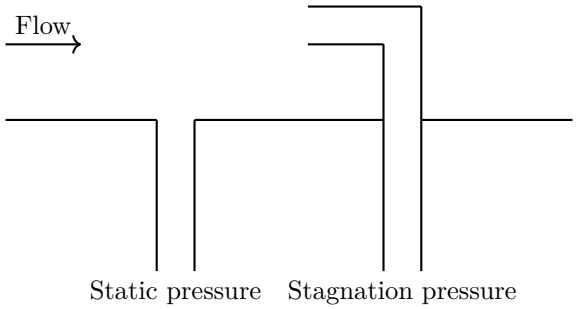

Figure 1: The figure shows how static and stagnant pressure of a flow is measured.

3 Methodology

The work started with designing a digital model in CAD and was then split into an experimental model and a numerical model. These parts were done in parallel as they are to a large extent independent of each other. At the end of the project the results between the two methods are compared.

3.1 Geometry of the model

The geometry of the train is based on a CAD model of the ICE3 train. This model was provided as part of the project and has been simplified slightly. The bulge of the front screen windows is removed and the model is made symmetric along both the x- and the y-axis. Here, the x-axis is the axis along the length of the train and the y-axis is in the direction of the width of the train. The finished model with its separate parts and measurements is depicted in Figure 2.

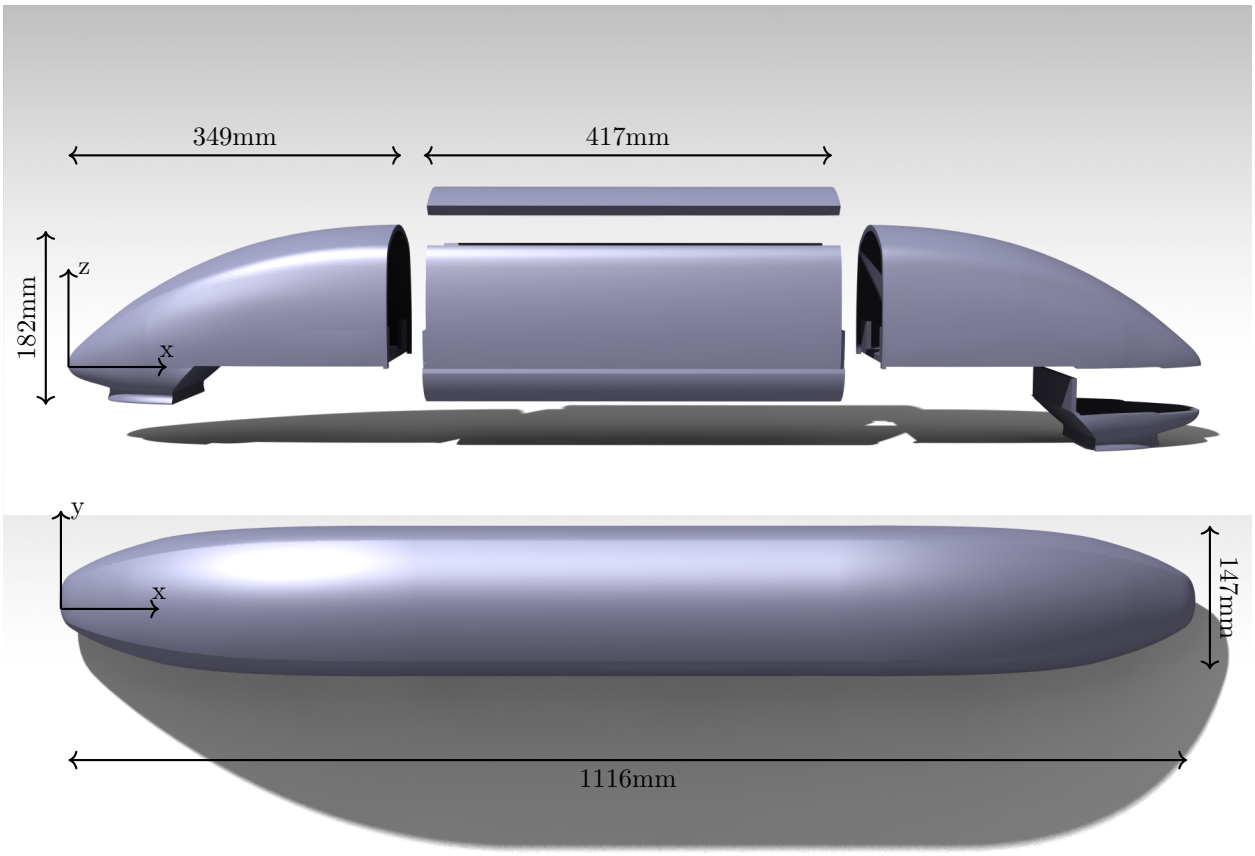

Figure 2: A picture displaying the different parts as well as the dimensions of the train.

3.2 Experiments

The experimental work consists of taking measurements of the physical model in a wind tunnel. Static pressure is measured using pressure taps at 13 points on the surface of the model. Using a Pitot-tube at the start of the test-section in the wind tunnel, a reference pressure and the dynamic pressure is measured.

These are used to calculate the stagnation pressure. The reaction force of the train is also measured using a force balance. Since the model is symmetric, the side force is not relevant in this project, although it is of course important to check that the set up is symmetric. Similarly, as the real train is heavy, the lift is insignificant and thus also excluded. At very high speeds the lift does have an influence, which introduces the need for studying the effect of ground clearance. The drag force however is an important measurement.

3.2.1 Design of the physical model

The model is split into four parts, two nose sections, one middle section and one roof. The parts are 3D printed using a *Modix Big60* 3D printer, one at a time. The printed parts are ground with sandpaper in order to get a smooth surface. The material used for 3D-printing is polylactic acid, or PLA. The nose and middle sections are screwed together and the gaps are closed using aluminium tape. The nose part was initially split into a top and bottom part. As a result the first nose that was printed is split in two and screwed together, tightening the gap with tape. The second nose that was printed however was printed as one piece as it gave a better result and shorter print time. The roof is only taped on and not screwed to the rest of the train. This makes it easy to remove and allows work inside the model. Holes for pressure taps are drilled and the taps, connected with tubes, are glued in place. The glue acts as both fastener and as an air tight seal around the pressure taps.

The model is seated on a support, in the shape of an airfoil, which is connected to the force balance in the wind tunnel. The shape of the support is chosen so the impact on the flow is minimised. The distance between the ground and the bottom of the unscaled train is given as 336mm [13]. This distance is called the ground clearance. For the scale model this means a ground clearance of 16.8mm. The model together with the support is shown in Figure 3. A hole on the inside of the support allows the tubes that connect to the pressure taps to exit the model without disturbing the flow. The tubing was then connected to a *Pressure Systems Pressure Scanner, model 9116*.

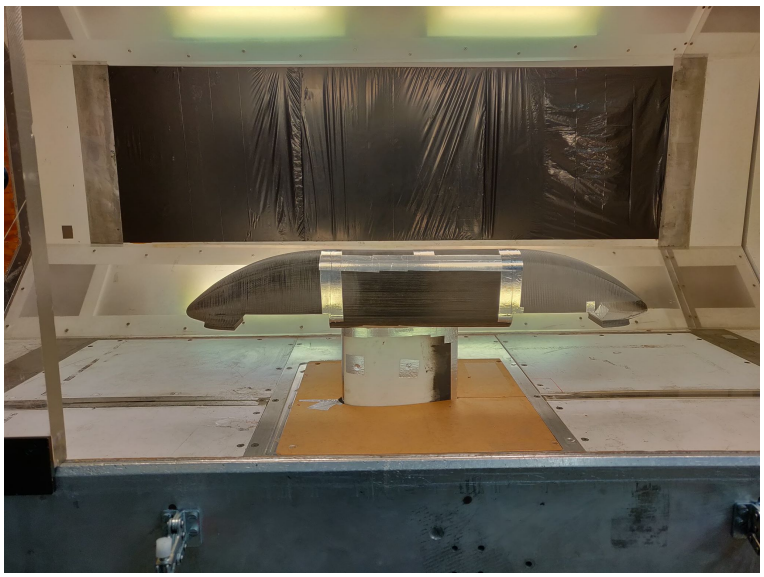

Figure 3: Placement of the model on the support inside of the wind tunnel. (Ground clearance not adjusted.)

3.2.2 Measurements

The measurements on the physical model are done using an airflow velocity of 25 m/s, 30 m/s, 35 m/s and 40 m/s. The flow is generated in a wind tunnel with a cross section of 1.28 m by 1.25 m and a length of 3 m.

The flow around the train creates pressures on its surface. These pressures are measured using pressure taps. Thirteen pressure taps are used in total. They are divided over the surface as shown in Figure 4. The pressure taps are numbered to easily keep track of which pressure tap placement generates which result. A reference pressure is also measured. This is done by measuring the pressure at the beginning of the wind tunnel using a Pitot-tube.

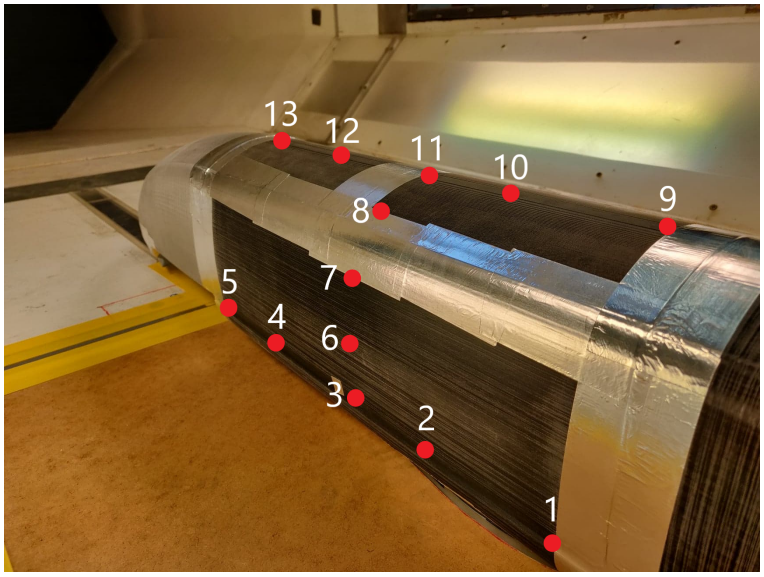

Figure 4: Placement of the pressure taps (red dots) on the scale model of the train. Note that the black nose is the front of the train, and the silver nose the back.

3.3 Numerical

In this section the methodology for the numerical part of the project is presented. The numerical part is an iterative process, where each part is executed several times. This is to ensure the quality of the mesh and to test different turbulence models and cases.

3.3.1 Geometry and boundary conditions

The simplified CAD model, described in chapter 3.1, is customized for the simulation. From the different parts of the train one whole surface is created with the same geometry. It is of great importance to get a fully enclosed geometry that can be used for creating the mesh in STAR-CCM+.

In STAR-CCM+ a flow domain is constructed. The flow domain is designed such that its dimensions are the same as the wind tunnel. The dimensions of the domain are expressed relative to the height of the train according to Figure 5. The height of the train, H, is 182 mm, as seen in Figure 2. In Figure 5 the inlet is located to the left of the domain and the outlet is located to the right.

The inlet is specified as a velocity inlet with a velocity of 25 m/s normal to the inlet. The outlet is specified as a pressure outlet with a gauge pressure of 0 Pa. This means that the outlet pressure is the same as the atmospheric pressure defined in the flow domain, which is 101325 Pa, or 1 atm. The top wall and the side walls are defined as symmetry planes and the ground is defined as wall. The reason the side walls are specified as symmetry planes rather than walls is to reduce the mesh size, as the cell size needs to be small at the walls. This is a reasonable assumption to make when the flow at the walls does not influence the flow at the model. In particular, this condition is fulfilled when the blockage ratio, the frontal area of the model over the frontal area of the domain is smaller than 0.05 [14]. For our model this ratio approximately corresponds to

$$\text{Blockage ratio} = \frac{A_{\text{model}}}{A_{\text{domain}}} = \frac{0.0245}{7.54} = 0.003. \tag{34}$$

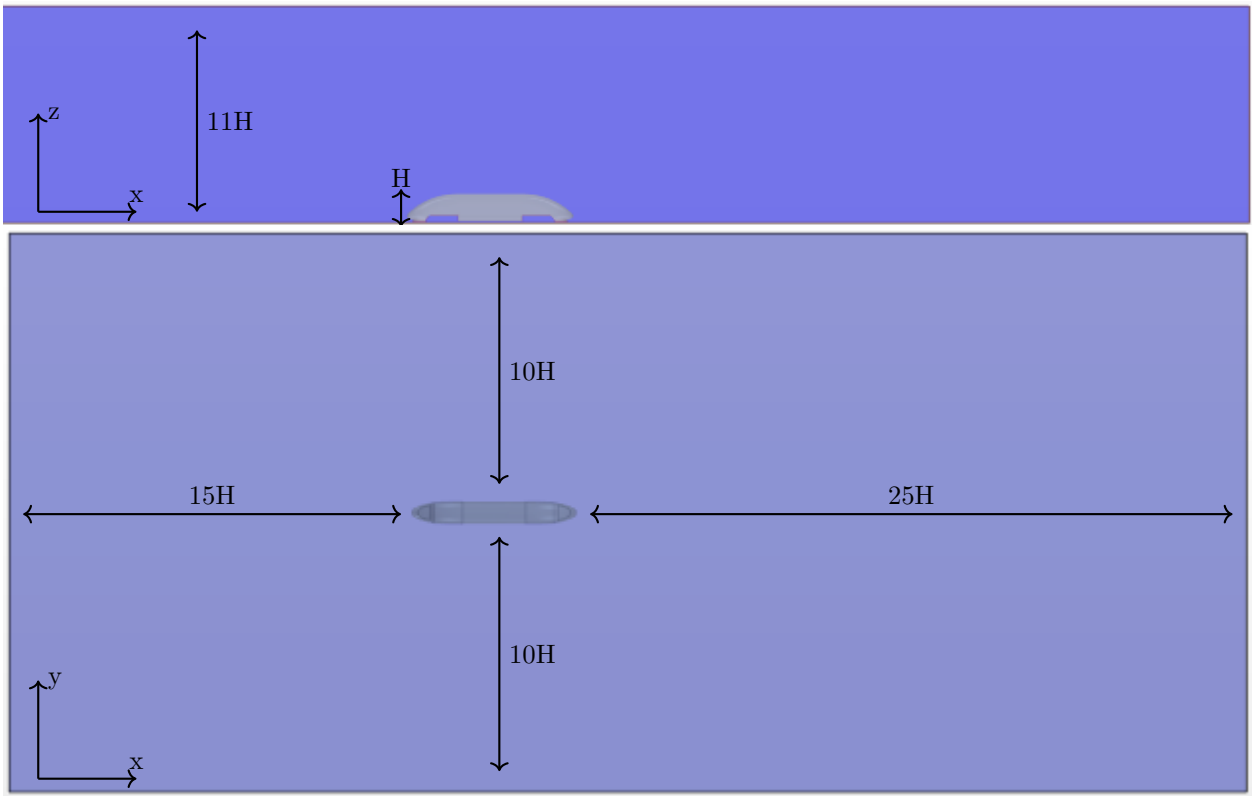

Figure 5: Side view and top view of the train inside the flow domain. The inlet is located to the left and the outlet to the right. H = 182 mm.

3.3.2 Mesh

For creating the mesh, the automated mesh function in STAR CCM+ is used. The choice of the volume mesher is based on the STAR-CCM+ documentation [7]. The polyhedral mesher and the prism layer mesher are used to generate the volume mesh for the geometry. The polyhedral mesher is chosen over the trimmed and the tetrahedral mesher. The trimmed mesher is not as dependent on the quality of the surface mesh, as the polyhedral and tetrahedral mesher. A trimmed mesher is therefore preferred when the geometry is complex and it is difficult to achieve a good quality surface mesh. However, considering the simplicity of

the geometry, a good quality surface mesh was achieved and therefore a trimmed mesher was not required to generate the volume mesh. The tetrahedral mesher uses quadratic elements, implying that the flux is computed through 4 faces. In comparison, the polyhedral mesher computes the flux through 5 faces, using polyhedral cells. The use of the polyhedral cells leads to more accurate results compared to tetrahedral cells. The use of a polyhedral mesh does not require any extra surface preparation when compared to a tetrahedral mesh. Furthermore, for a tetrahedral mesh to achieve the same accuracy as a polyhedral mesh, the former requires five to eight times greater number of cells. Therefore, despite the fact that the flux is calculated over one extra face per cell, the polyhedral mesher is computationally less expensive, when the goal is to achieve the same accuracy. Therefore the polyhedral mesh is chosen over the other meshers.

Intuitively the flow is expected to separate behind the train. However, due to the aerodynamically streamlined shape of the geometry, the flow separation is expected to be minimum and the flow is expected to re-attach to the model quickly. To resolve the wake region behind the train, the wake refinement function within Star-CCM+ is used. This function enables the user to independently control the meshing in the wake region, which is an important area for this flow, as discussed previously. A wake region is also implemented for the two cavity regions below the train.

The other area of focus is the near wall regions. A boundary layer develops in this region, as a result of the no-slip condition. There are two different ways to treat the wall boundaries. The first way is to use wall functions, referred to as the high-y^+ wall treatment. When using high-y^+ wall treatment the first cell centre should be be located at $y^+ > 30$. This allows the use of a coarse mesh, but is not very accurate. A more accurate method is to use a fine mesh at the wall boundaries with the first cell size such that $y^+ < 1$. This is called low-y^+ treatment. This requires a mesh fine enough to resolve the boundary layer without wall functions. The prism layer mesher is used to mesh the wall boundary layer, i.e, the train surface and the floor of the wind tunnel. The all-y^+ model was used in Star-CCM+, to determine the use of wall-functions in the near wall regions. This is a hybrid model and uses low-y^+ treatment when the mesh is fine enough and high-y^+ wall treatment otherwise [7].

An initial guess on the first prism layer thickness to get $y^+ < 1$ at the wall, is calculated using Equations 28 and 29. $y^+ < 1$, to ensure no wall functions are used at the walls. $y^+ = 1$ is assumed for the first guess of the cell size. The prism layer is then modified if y^+ is found to be greater than one. The number of prism layers is chosen with respect to the growth ratio. The growth ratio of the cells throughout the mesh is 1.2, to limit the sudden growth of cells. The prism layer overall thickness and the number of prism layers are controlled to achieve a good growth ratio between the last prism layer cell and the first polyhedral cell adjacent to it, also to prevent any sudden jump in cell size.

The other factor to be considered while generating the mesh is the cell size of the first cell in the streamwise and spanwise direction, Δ_s^+ and Δ_l^+, respectively. The aforementioned quantities are computed using equation 30 and equation 31. As mentioned previously, ideally $\Delta_s^+ < 1000$ y^+ and $\Delta_l^+ < 300$ y^+. While generating a coarser or finer mesh the average wall y^+ needs to be maintained nearly constant and the refinement must be achieved by varying Δ_s^+ and Δ_l^+.

3.3.3 Simulation

The simulation is done using STAR-CCM+. The first step is to try two different turbulence models to compare which one works best for this case, $k - \epsilon$ or $k - \omega$. The following settings for the physics in STAR-CCM+ are used for both turbulence models:

- Three dimensional
- Steady
- Gas: air with $\rho = 1.18415[kg/m^3]$ and $\nu = 1.85508 \times 10^{-5}[Pa - s]$
- Segregated flow

- Gradients
- Turbulent
- Constant density
- Reynolds-Averaged Navier-Stokes
- Exact wall distance
- Proximity interpolation

As mentioned, the two turbulence models are $k-\epsilon$ and $k-\omega$ with the following settings:

$\underline{k-\epsilon}$

- Realizable k-epsilon two-layer
- Two-layer all y+ wall treatment

$\underline{k-\omega}$

- SST (menter) k-omega
- All y+ wall treatment
- Gamma transition

The next step in the simulation procedure is to perform a mesh independence study using three different meshes, a coarse, medium and fine grid. This is done using 16.80 mm (0.0923 H) ground clearance. This independence study is used to find a mesh resolution that is as coarse as possible, to minimize computational time, but fine enough to ensure that the results do not change when using a different, finer, mesh. Once the suitable mesh resolution is decided, two more cases are simulated with ground clearance 8.65 mm (0.0475 H) and 24.70 mm (0.1357 H).

3.4 Comparison of data

A comparison between simulation and experiment is also needed. This is done with both body forces as well as static pressure on the surface. The pressure had to be normalized using the stagnation pressure of each domain. In the computational case, this is equal to the pressure at the nose of the train. This assumption can be made as the flow at the front of the nose is normal to the surface and stagnates here. In the experimental case, the stagnation pressure is acquired from the Pitot tube in the reference point. The actual stagnation pressure at the Pitot tube is never explicitly recorded, however, the static and dynamic pressure is. The stagnation pressure is then calculated using equation 33.

3.5 Analysis of ground clearance

The main advantage of CFD is that, once the numerical model is validated it can be used to analyze different configurations in more detail without having to do the experimental work. This makes further research significantly easier. In this project one example of such further research is considered, the influence of the distance between the ground and the bottom of the train. To do this two different ground clearances were considered, 494 mm and 173 mm. These are chosen as they are the same ground clearances as used for a similar model [13]. For our scale model this results in ground clearances equal to 24.7 mm (0.1357 H) and 8.65 mm (0.0475 H).

4 Validation and Results

In this section the results of the experimental and numerical work are presented. After considering the experimental and numerical results separately, the two different methods are compared in order to validate the numerical model. Finally, the influence of the height between the ground and the train is analyzed using the validated numerical model.

4.1 Experimental results

The general results of the wind tunnel experiments can be found in Table 1. Since it is not possible to control the flow velocity in the wind tunnel accurately, a more precise value of the velocity is given here as well. This highlights the importance of using the pressure and drag coefficients, rather than comparing pressure and drag force directly, to minimize the influence of these small differences on the results. Here the values of the side-forces are also given. Because these forces are low, it can be concluded that the set-up is reasonably symmetric.

Furthermore, it becomes clear that the Reynolds number is significantly over 250 000 for all flow velocities. These results are thus comparable to the results that would be obtained when a real train would be used instead of the scale model. Here the drag force, and drag coefficient, can also be found for the different velocities. It is clear that as the velocity increases the drag force increases as well. The drag coefficient however, stays relatively constant. The lift is disregarded here as it is significantly influenced by the support and is thus not comparable to the numerical results.

The results from the pressure taps are presented in Table 2. Here it can be seen that the pressure changes significantly for different velocities. However, similar to the drag coefficients, the pressure coefficients stay relatively constant.

Table 1: Results of the wind tunnel experiments for different wind velocities.

	25 [m/s]	30 [m/s]	35 [m/s]	40 [m/s]
ν [m^2/s]	1.55×10^{-5}	1.55×10^{-5}	1.55×10^{-5}	1.56×10^{-5}
ρ [kg/m^3]	1.18	1.18	1.18	1.18
u [m/s]	25.0	30.1	35.2	40.4
Re	293×10^3	353×10^3	412×10^3	471×10^3
F_s [N]	-0.04	-0.11	-0.20	-0.12
F_d [N]	2.797	3.858	5.310	7.309
c_d	0.309	0.311	0.297	0.295
p_{stag} [N]	450	626	861	1131

The experimental setup created some turbulence at the sides of the train. This problem most likely arises primarily due to the airfoil support, the rough floor and the small gaps and edges in the model. Figure 6 (c) and (d) show that the flow is detached at the sides of the train. See Figure 6 (e) and (f) for a clearer view of the tufts. The detachment can be seen from the tufts which are in different positions in the different pictures, which are taken at different instances of time for the same test case. This behavior is particularly clear for the last tuft (#9) on the right side which seems flapping energetically. The flow is however attached along the roof, as can be seen in Figure 6 (a) and (b).

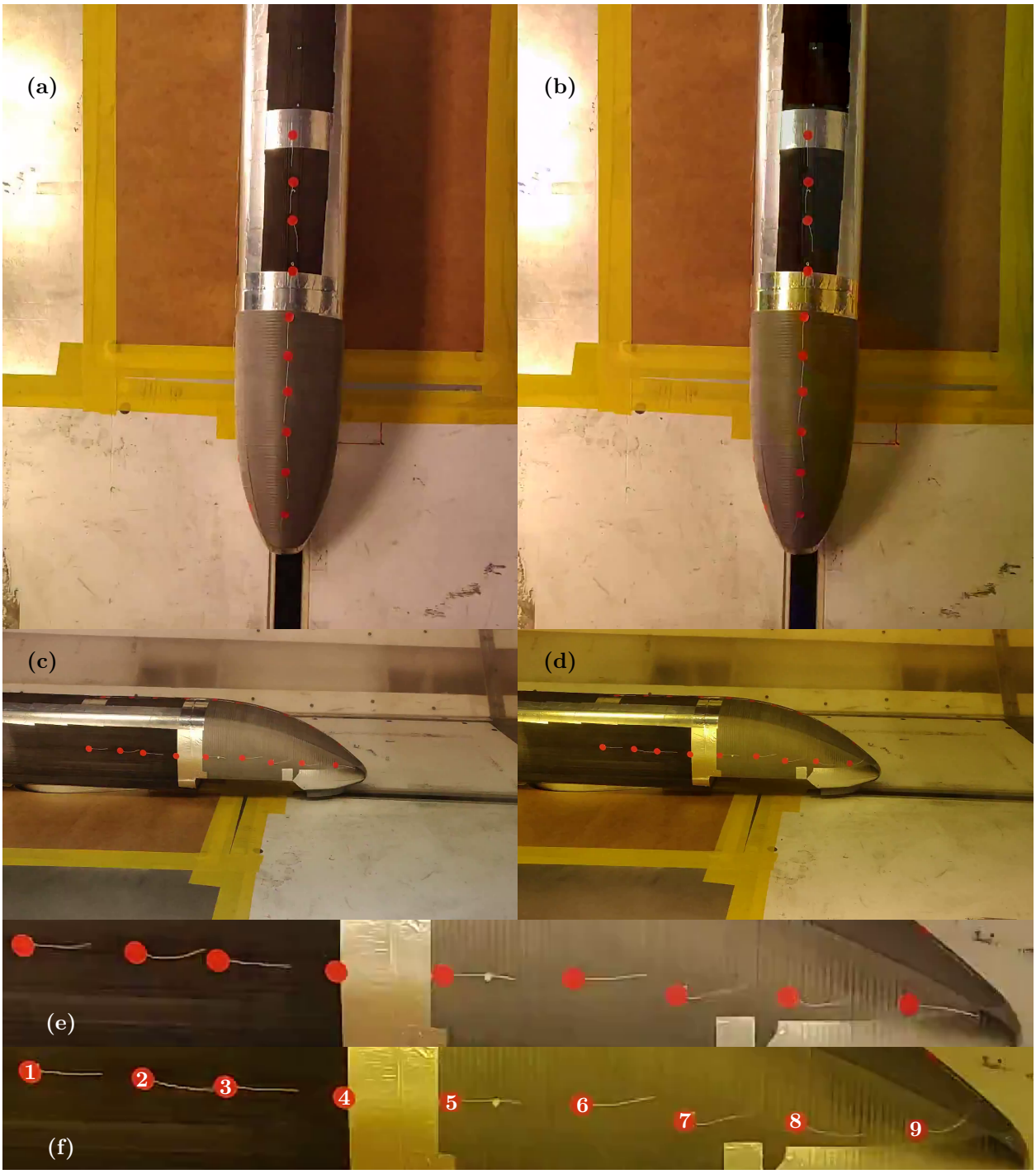

Figure 6: Assessing air flow around the train using tufts. The differing lighting in the pictures is from the camera frame-rate not matching up with the lightening frequency. (a) and (b) show the top view, (c) and (d) the side view and (e) and (f) a zoom in of the side view at different times.

Table 2: Results of the pressure taps during the wind tunnel experiments for different wind velocities.

	25 [m/s]		30 [m/s]		35[m/s]		40 [m/s]	
	p [Pa]	c_p	p [Pa]	c_p	p [Pa]	c_p	p [Pa]	C_p
p_1	0.241	-0.217	-21.625	-0.212	-29.767	-0.216	-64.928	-0.243
p_2	14.903	-0.178	-2.061	-0.176	-2.573	-0.179	-9.877	-0.186
p_3	5.330	-0.204	-20.052	-0.209	-30.363	-0.217	-44.424	-0.222
p_4	40.344	-0.109	28.835	-0.118	43.314	-0.116	56.471	-0.117
p_5	48.068	-0.088	43.097	-0.091	64.464	-0.087	86.185	-0.086
p_6	24.607	-0.151	13.748	-0.146	21.249	-0.146	24.247	-0.150
p_7	24.138	-0.153	11.916	-0.149	17.958	-0.151	21.210	-0.153
p_8	55.640	-0.067	48.988	-0.080	69.779	-0.080	90.916	-0.081
p_9	15.996	-0.175	-1.868	-0.175	4.764	-0.169	34.980	-0.139
p_{10}	35.582	-0.122	25.770	-0.124	36.805	-0.125	48.067	-0.126
p_{11}	48.094	-0.088	40.191	-0.097	58.134	-0.096	78.347	-0.094
p_{12}	43.341	-0.101	38.055	-0.101	55.142	-0.100	71.974	-0.101
p_{13}	34.647	-0.124	17.097	-0.140	27.978	-0.137	37.136	-0.137
p_∞	80.517	0.000	91.756	0.000	128.47	0.000	168.852	0.000

4.2 Mesh independence study

Using the methods described in section 3.3.2 in Star-CCM+ three different meshes are created, with varying number of cells. To compare the meshes the number of cells are changed by $\pm 20\%$. The properties of the three meshes are presented in Table 3. The mesh independence study is carried out using these three meshes.

Table 3: Mesh Comparison.

	Coarse Mesh	Medium Mesh	Fine Mesh
Total Cells	2.53 Million	3.12 Million	3.65 Million
Number of Prism Layer	15	18	18
Prism Layer Thickness	0.025H $\sim$ 0.03H	0.025H $\sim$ 0.03H	0.025H $\sim$ 0.03H
Wake Region Length	1.0m	1.0m	1.0m
Cell Size - Wake Region Refinement	0.1H	0.08H	0.06H
Cell Size - Under Body Refinement	0.02H	0.02H	0.01H
Train Surface Wall_Y+	~ 1	~ 1	~ 1
Average Train Surface Wall_Y+	0.37	0.37	0.37
Δ_s^+	227	207	203
Δ_l^+	232	205	204

They are compared using velocity profiles in the wake region and the left bogie cavity, the c_p values along the mid-line of the train and the total drag experienced by the model. The bogie cavities are the holes at the bottom of the train, where there is room for the bogie group. The drag values experienced by the train model are presented in Table 4. Figure 7 illustrates the c_p and the velocity profiles at the two different regions mentioned above.

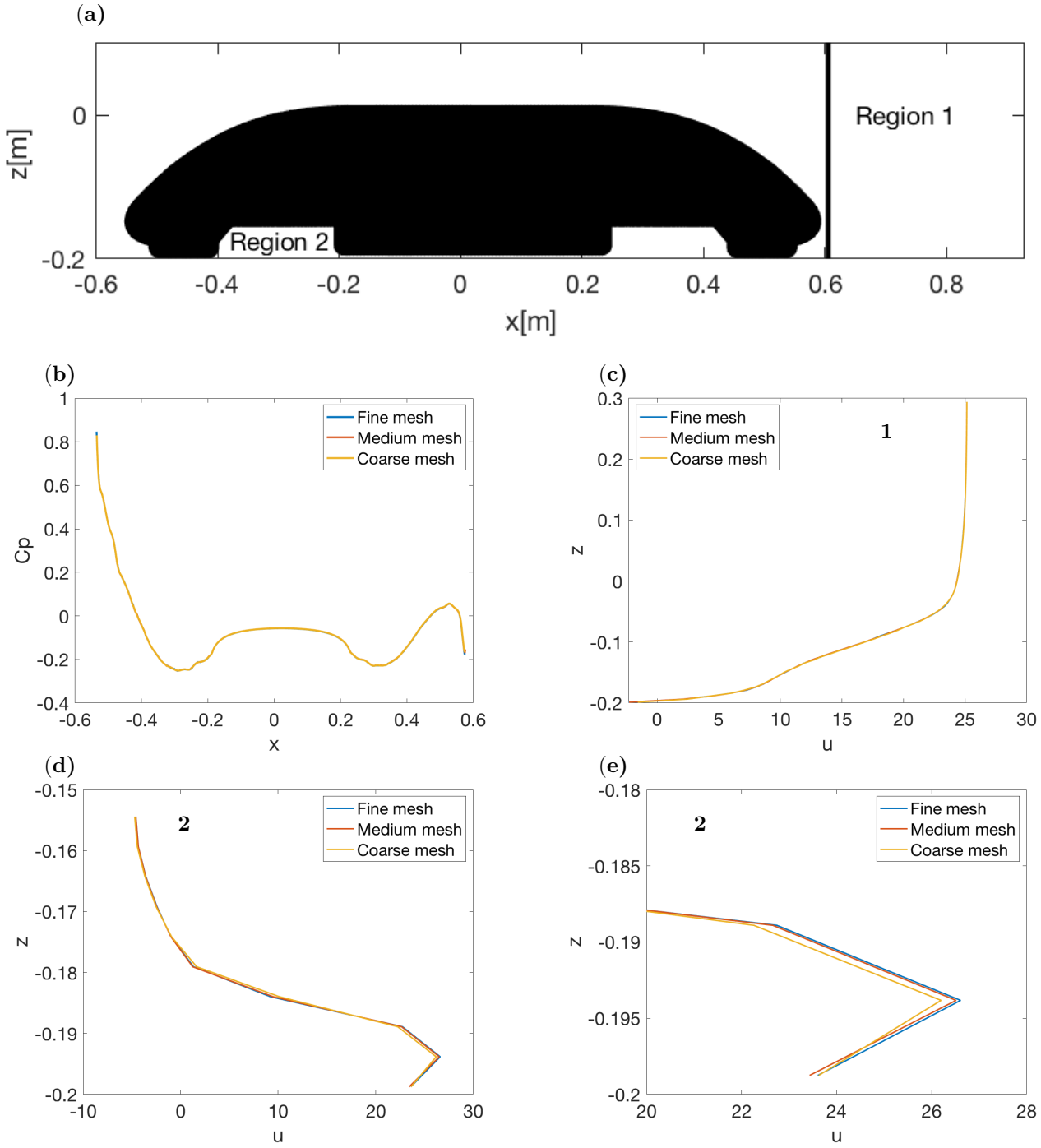

Figure 7: Mesh Independence Study: (a) Schematic of train regions being assessed (b) c_p along mid-line of the train, measured at the train surface from the front to the rear (c) Velocity profile wake region, z=0 is located at the roof of the train (d) Velocity profile bogie at Region 2 (e) Zoomed in Velocity Profile at Region 2.

Table 4: Mesh Independence Study: Drag Force Comparison.

	Coarse Mesh	Medium Mesh	Fine Mesh
Drag Force [N]	2.50	2.49	2.48

There is no significant change observed in the drag force values, c_p profile and velocity profile in the wake region for the three different meshes. However, in the left bogie cavity, a small difference can be observed in the velocity profile for the coarse mesh, as seen in Figure 7 (c) and Figure 7 (d). Therefore, the coarse mesh is not considered for further simulations. However, for all regions the medium and the fine mesh yield the same result. The choice between the medium and the fine mesh is made on the basis of computational resources. The computational resources required by the medium mesh would be lower than the fine mesh. The medium mesh is selected for all further simulations. The medium mesh is displayed in Figure 8.

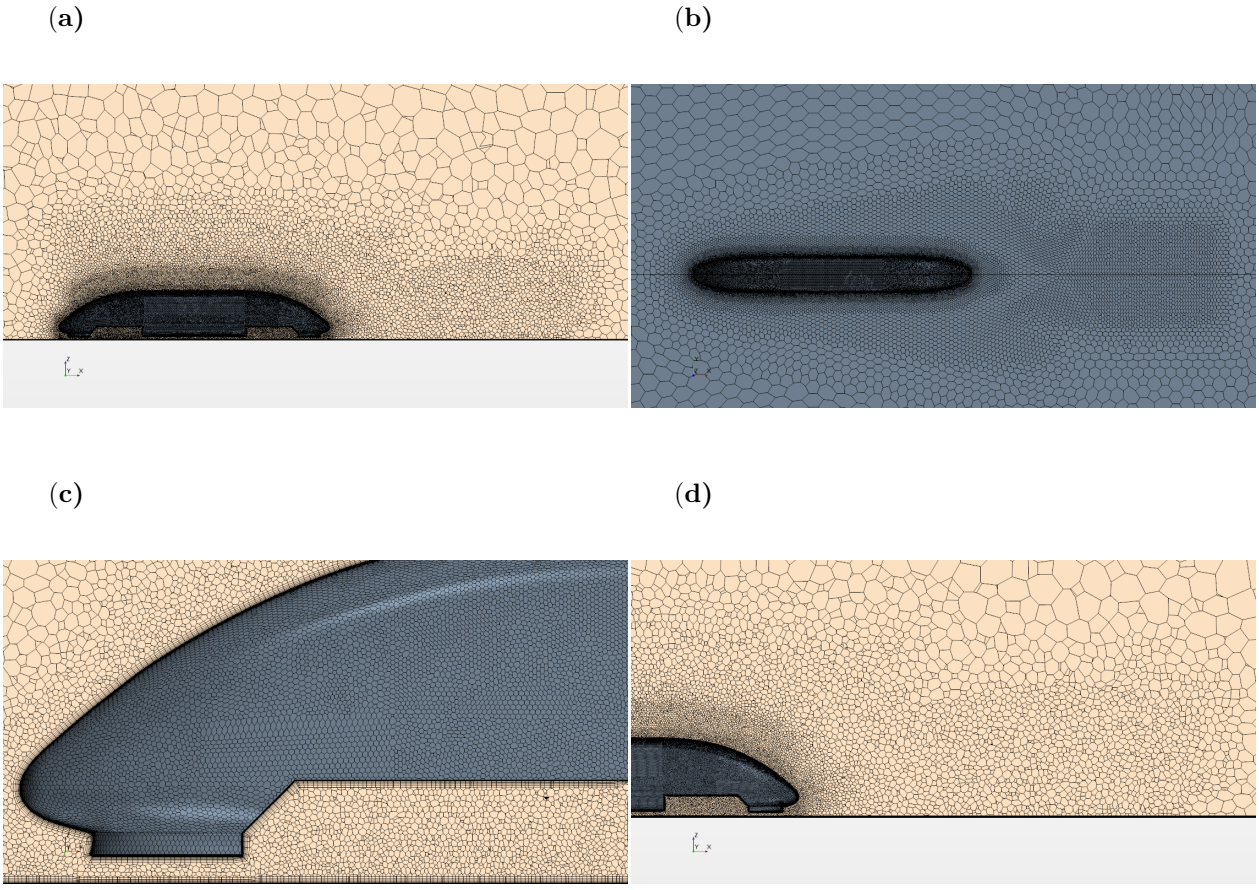

Figure 8: Medium Mesh: (a) Mesh Left View (b) Mesh Top View (c) Underbody Mesh (d)Wake Refinement Region.

4.3 Choice of turbulence model

The first step regarding the simulation is to decide which turbulence to proceed with, $k-\epsilon$ or $k-\omega$ SST. Therefore, a simulation of the same case is done with both models. When comparing the contour plots of the velocity in x-direction, the results are similar. However, a pressure plot on the surface of the train shows that the pressure is asymmetric when using $k-\omega$ SST as turbulence model. This can clearly be seen from below as shown in Figure 9. The reason for the fluctuations in pressure may depend on that $k-\omega$ is not an isotropic solver. Therefore, it does not find a steady state solution for the Navies Stokes equations. Instead it oscillates between possible steady state solutions generated by a typical vortex shredding behind the train. This could be solved by taking the solutions from several iterations and then averaging, instead of only using the solution from the last iteration. However, when using the $k-\epsilon$ model the contour plot of the surface was symmetric, meaning that no unwanted fluctuations occurred. This is a result of $k-\epsilon$ model being an isotropic solver.

One of the reasons to use $k-\omega$ SST instead of $k-\epsilon$ is that it is more accurate when the boundary layer approaches separation. However, since the train is a streamlined body there is no significant flow separation present. Therefore the $k-\epsilon$ model works reasonably well. Because of this and the fluctuations of the $k-\omega$ SST model, the $k-\epsilon$ model is the turbulence model of choice to proceed with.

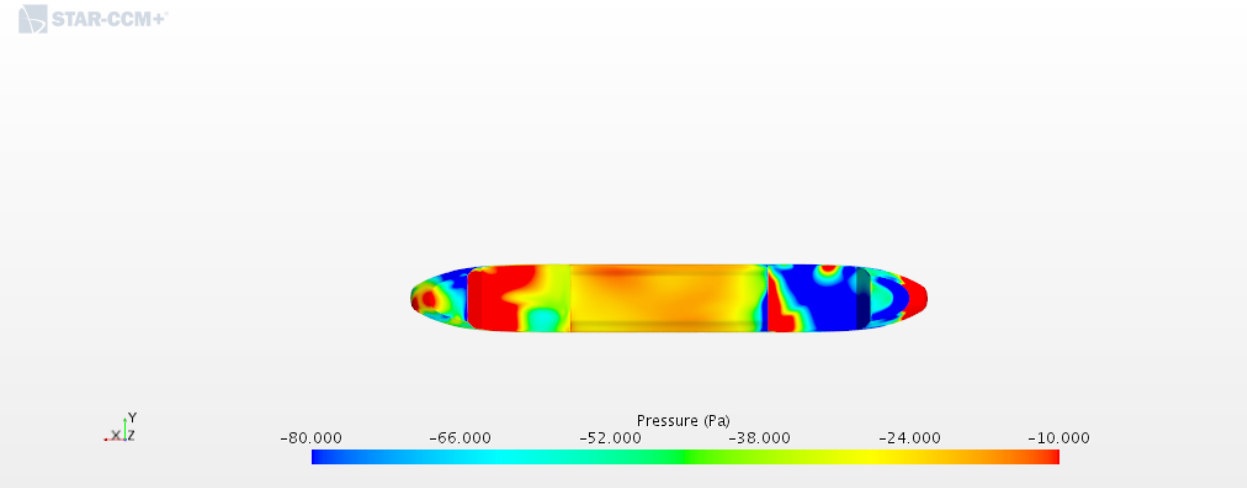

Figure 9: Pressure on the bottom of the train surface.

4.4 Numerical results and their comparison to experimental results

In this section the numerical result is presented and subsequently compared with the experimental results to validate the CFD model.

4.4.1 Pressure comparison

One of the results that can be compared between the experimental and numerical model is the pressure. To get a good comparison the static pressure can not be compared directly but the pressure coefficient, c_p, is compared instead. It is calculated using Equation 2 in each of the pressure tap locations. The size of the error is then calculated as

$$\text{Err} = \frac{c_p^{num}}{c_{p,max}^{num}} - \frac{c_p^{exp}}{c_{p,max}^{exp}} \tag{35}$$

for a certain point in the domain. $c_{p,max}^{num}$ is calculated at the stagnation point at the front of the train and $c_{p,max}^{exp}$ is calculated from the static and stagnation pressure from the Pitot tube in the free stream flow. The resulting error can be seen in percentage in Figure 10. As can be seen, the error along the roof of the train is quite small, between 2.7% and 5.6% in the measured points. On the sides however the error is larger, with error values up to 14.9% in the measured points. This is likely caused by the airfoil support that is not included in the numerical simulations. This is further supported by the error being larger where the airfoil is thick and smaller where it is thin or even no longer present. See Figure 3 for the airfoil position.

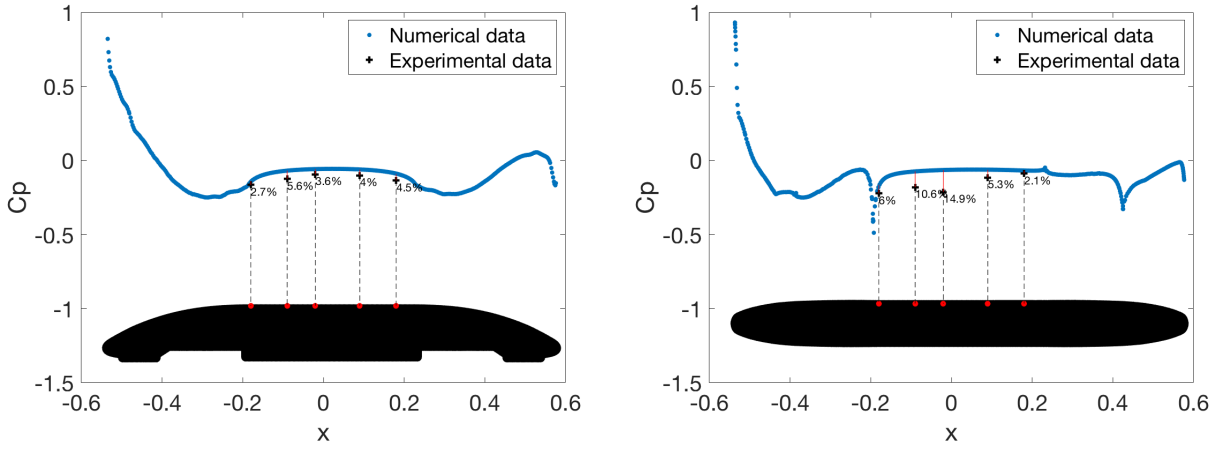

Figure 10: A comparison between numerical and experimental c_p values in the roof (left) and the side (right) of the train. The size of the error is also shown in percentage.

4.4.2 Drag comparison

Another way to check the validity of the CFD model is to compare the dimensionless drag coefficient. This is computed according to Equation 1. When calculating the drag coefficient for the experimental result four different velocities are used, 25 m/s, 30 m/s, 35 m/s and 40 m/s. These four velocities result in four drag forces, which are used to calculate the corresponding drag coefficients. This is then averaged to get the final drag coefficient for the experimental result.

In Table 5 the experimental data obtained from the wind tunnel experiment is compared to the numerical data obtained from the CFD simulations. A percentage error of 9% between the experimental and the numerical data is observed. This error can be explained by that the train in the wind tunnel uses a support, which is not used in the numerical simulation. The support contributes to a larger drag force, which will lead to a higher c_d value for the experimental data.

Table 5: Drag coefficient Comparison: experimental and numerical.

	Experimental	Numerical	Error [%]
C_d	0.303	0.276	9

4.4.3 Streamline comparison

In Figure 11 the streamlines are plotted on the train. This Figure is compared to Figure 6 which shows the train with the tufts. According to Figure 6 the streamlines should be in the flow direction on the roof of the

(a) (b)

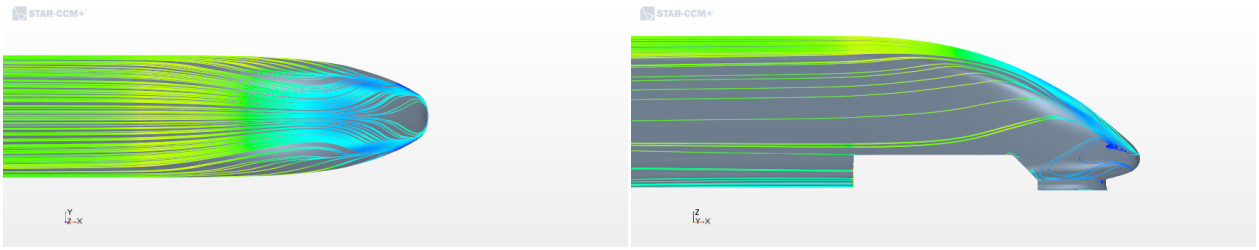

Figure 11: Streamlines, rear part of the train: (a) top view (b) left view.

train. This make sense due to symmetry and is true in the CFD simulation as well. As explained in chapter 4.1 there was some turbulence in the wind tunnel experiment. This makes it difficult to compare the side tufts with the streamlines, however they point mainly in the same direction as the streamlines.

4.5 Dependence on ground clearance

Three different ground clearances are tested including the first one of 0.0923 H. The result in the form of drag and lift forces can be found in Table 6 below. The comparison clearly shows that both the drag and lift forces increases with increased ground clearance. The increase in drag force can be explained comparing Figure 12 and 13. Here, it is clear that the pressure at the back of the bogie cavity is significantly higher for the high ground clearance than it is for the low ground clearance. These regions of higher pressure obviously result in a higher drag force over the whole train. The increase in lift force can be explained by comparing Figure 12 and 13 together with Figure 14. The pressure on top of the train does not change considerably when increasing the ground clearance. However, the pressure on the bottom of the train is significantly higher with the higher ground clearance, as can be seen in Figure 14. Thus, the net pressure change will increase the lift force with higher ground clearance.

The reason for these differences due to the ground clearance becomes clear when considering Figures 15 and 16. When the ground clearance is high there is more room for the fluid to go between the train and the ground. Because of this, more fluid collides with the edge of the bogie cavities, resulting in a higher pressure regions. When the ground clearance is low the fluid flow between the ground and the train is very low instead. What results is a lower pressure and lower drag and lift forces.

Table 6: Dependence of ground clearance: drag and lift force comparison.

Ground clearance	0.0475 H	0.0923 H	0.1357 H
Drag Force [N]	2.06	2.49	2.64
Lift Force [N]	0.06	0.52	2.97

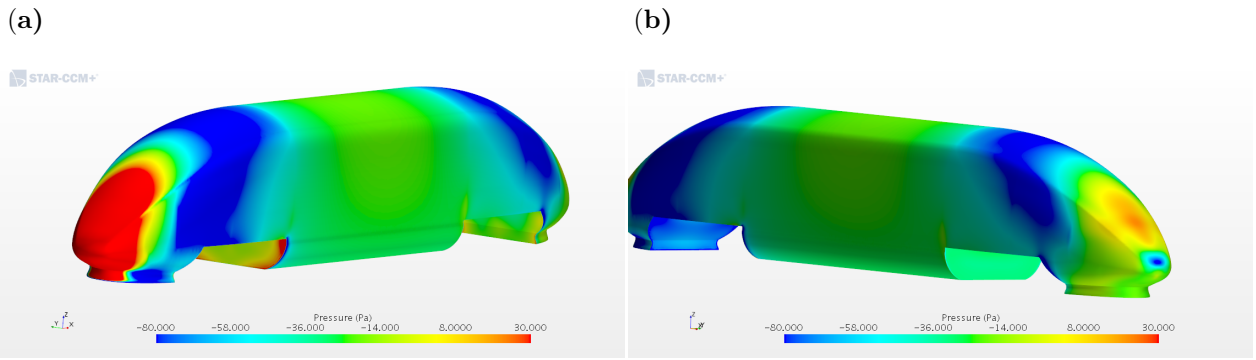

Figure 12: Pressure on the surface of the train at 0.0475 H ground clearance: (a) front (b) rear.

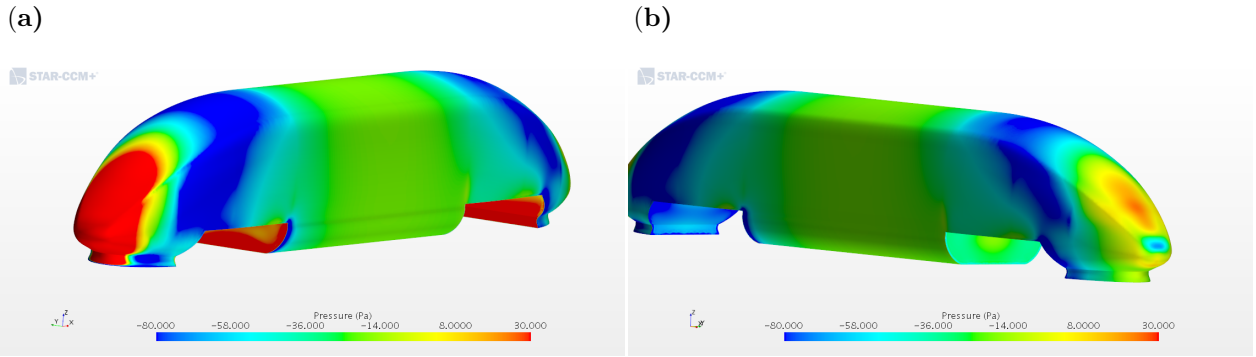

Figure 13: Pressure on the surface of the train at 0.1357 H ground clearance: (a) front (b) rear.

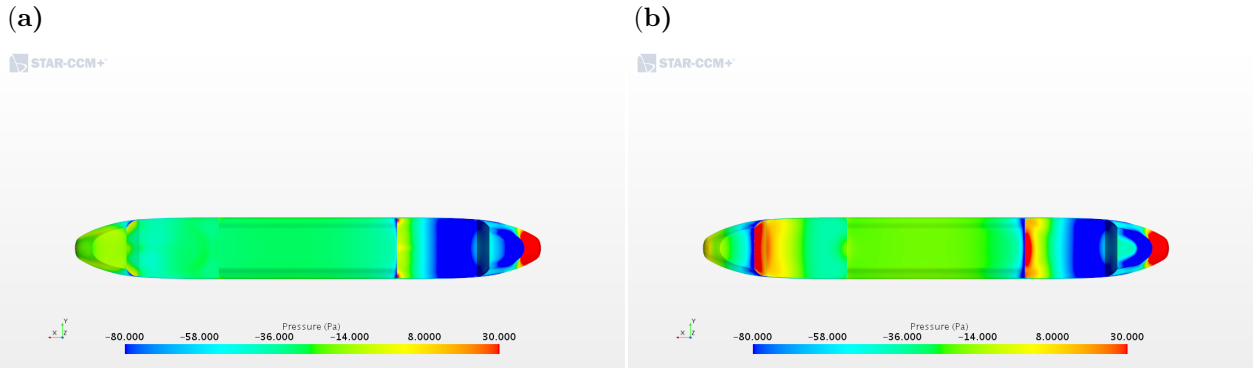

Figure 14: Pressure on the bottom of the train: (a) 0.0475 H ground clearance (b) 0.1357 H ground clearance. Do note that the flow direction is from right to left.

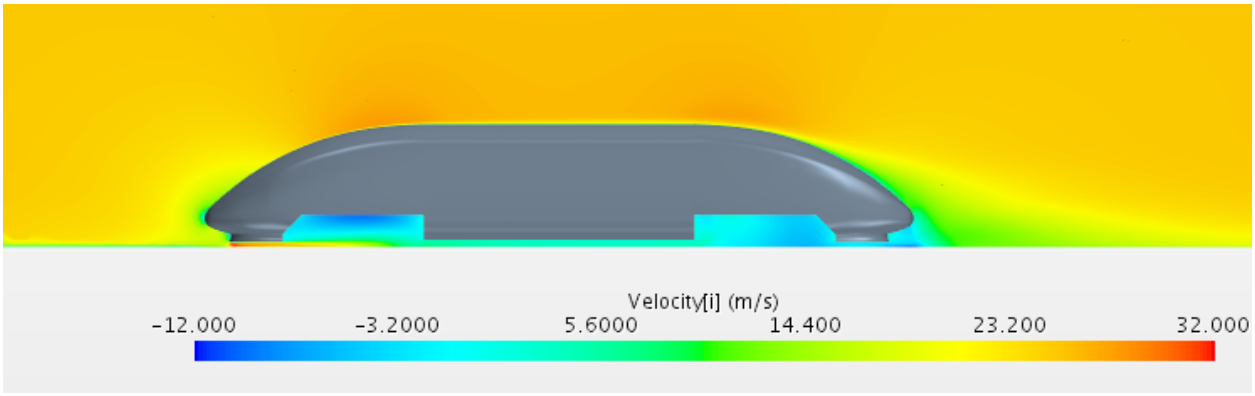

Figure 15: Velocity in x-direction around train with 0.0475 H ground clearance.

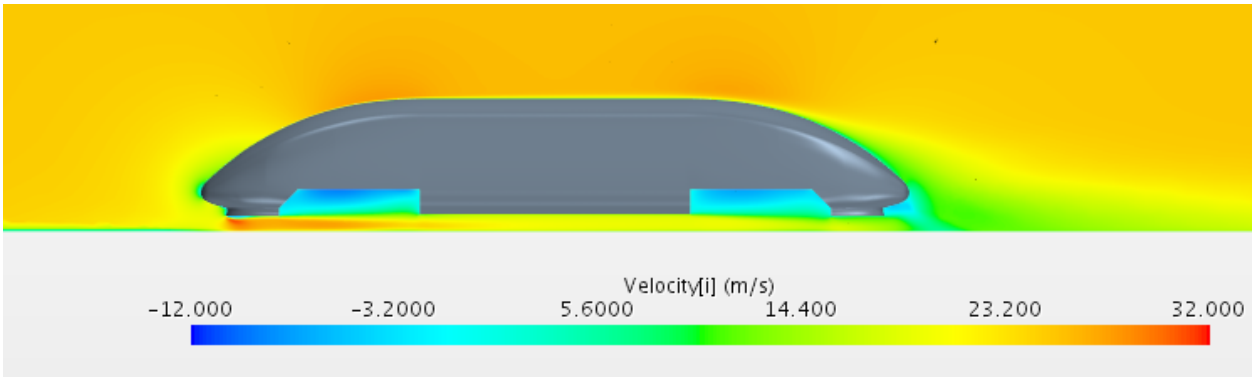

Figure 16: Velocity in x-direction around train with 0.1357 H ground clearance.

5 Conclusion and further outlook

A generic ICE3 train model was designed and tested with the main goal to validate a numerical CFD model. The verified model was used to determine the influence of the ground clearance effect on the drag and lift forces of the train.

To make the experiment possible a scale model of the ICE3 train was designed and created. This scale model was placed in a wind tunnel for experimental testing. Here the pressure at certain places of the model was measured, as well as drag and lift forces. The CFD simulations were performed using the realizable $k-\epsilon$ two-layer model and the $k-\omega$ SST model. However the $k-\omega$ SST model gave asymmetric results. Thus, the realizable $k-\epsilon$ two-layer model was chosen.

By comparing the numerical and experimental results it was concluded that the numerical model captured the present physics reasonably well. The deviation in pressure was on average 4.1% on the top of the train and 7.8% at the side of the train. The conclusion was that the higher deviation at the side of the train compared to the roof was due to the influence of the support that was used in the wind tunnel. This influence is higher than initially considered. Possibilities to resolve this would be to add the same support to the numerical model, or to reduce the size of the support so it interferes less with the flow. It also turns out that the location of the pressure taps on the experimental model was poorly chosen, as the value of c_p is consistently low throughout the entire area where the taps are placed. By using the results of the numerical model the pressure taps can be moved to more strategic locations. There is also a concern that the used turbulence model might not capture the physics well enough. Trying more turbulence models could produce a better comparison of the results. Particularly interesting would be to use an unsteady model, like LES, as both turbulence models considered in this project were steady RANS models. Finally the comparison between our models and a real train could be improved by suspending the train from above in the wind tunnel and placing a moving ground below it. By running this treadmill at the flow velocity one creates a more realistic environment, as it removes the boundary layer at the floor.

Using the validated numerical model, two more ground clearances were considered. It was found that both the drag and lift forces were reduced when reducing the ground clearance for the researched distances. When comparing the pressure it was found that the pressure was increased in the bogie cavities when increasing the ground clearance. This explained the higher drag and lift forces. Further research needs to be done to analyze whether this changes when bogies are installed in the bogie cavities.

The goal of this project was to manufacture a simplified physical model of an ICE3 train, to use it to validate a numerical model and to conduct a first numerical study on the ground clearance. The model designed in this project can be used for further research. One possibility was to further analyze the influence of the ground clearance by considering more values for the ground clearance. Other research possibilities include the influence of different types of boogies and the influence of the yaw angle on the train. Despite the possible improvements mentioned earlier in this section, this group considers the project goals to be achieved.

References

[1] Noise-induced hearing loss. https://www.nidcd.nih.gov/health/noise-induced-hearing-loss, 2017. [Online; accessed 17-May-2019].

[2] J.R. Bell, D. Burton, M.C. Thompson, A.H. Herbst, and J. Sheridan. Flow topology and unsteady features of the wake of a generic high-speed train. *Journal of Fluids and Structures*, 61:168 – 183, 2016.

[3] Hassan Hemida and Siniša Krajnović. Les study of the influence of the nose shape and yaw angles on flow structures around trains. *Journal of Wind Engineering and Industrial Aerodynamics*, 98(1):34 – 46, 2010.

[4] Shibo Wang, David Burton, Astrid Herbst, John Sheridan, and Mark C. Thompson. The effect of bogies on high-speed train slipstream and wake. *Journal of Fluids and Structures*, 83:471 – 489, 2018.

[5] High-speed trainset velaro d (class br 407). https://www.siemens.com/press/pool/de/feature/2013/infrastructure-cities/2013-12-ice/factsheet-high-speed-trainset-velaro-e.pdf, 2013. [Online; accessed 17-May-2019].

[6] *Railway Applications—Aerodynamics—Part 4: Requirements and Test Procedures for Aerodynamics on Open Track*. CEN European Standard, cen en 14067-4 edition, 2013.

[7] *STAR-CCM Documentation*. Siemens Product Lifecycle Management Software Inc, 2019.1 edition, 2019. [Online; accessed 10-May-2019].

[8] Lars Davidson. Fluid mechanics, turbulent flow and turbulence modeling. http://www.tfd.chalmers.se/~lada/comp_turb_model/postscript_files/solids-and-fluids_turbulent-flow_turbulence-modelling_25mars_2019.pdf, 2019. [Online; accessed 10-May-2019].

[9] F. R. Menter. Two-equation eddy-viscosity turbulence models for engineering applications. *AIAA Journal*, 32(8):1598–1605, 1994.

[10] Frank M. White. *Fluid Mechanics*. McGraw-Hill Education, seventh edition in si units edition, 2011.

[11] Set-up of a les around a notchback ahmed body. [Internal report; accessed 20-April-2019].

[12] Oxford English dictionary, Static pressure. https://en.oxforddictionaries.com/definition/static_pressure, 2019. [Online; accessed 15-May-2019].

[13] Tianyun Dong, Guglielmo Minelli, Jiabin Wang, and Sinisa Krajnovic. The effect of ground clearance on the aerodynamic characteristic of a general train. 2019. Article in progress.

[14] T.Y. Chen and L.R. Liou. Blockage corrections in wind tunnel tests of small horizontal-axis wind turbines. *Experimental Thermal and Fluid Science*, 35(3):565 – 569, 2011.